Topography of Extracellular Matrix Mediates Vascular Morphogenesis and Migration Speeds

Amy L. Bauer
Department of Mathematics,
University of Michigan, Ann Arbor, Michigan

Trachette L. Jackson
Department of Mathematics,
University of Michigan, Ann Arbor, Michigan

Yi Jiang [1]
Theoretical Division, Los Alamos National Laboratory,
Los Alamos, New Mexico

[1]Corresponding author. Address: Theoretical Division, MS B284, Los Alamos National Laboratory, Los Alamos, NM 87545. Tel.: (505)665-5745, E-mail: jiang@lanl.gov

Abstract

The extracellular matrix plays a critical role in orchestrating the events necessary for wound healing, muscle repair, morphogenesis, new blood vessel growth, and cancer invasion. In this study, we investigate the influence of extracellular matrix topography on the coordination of multi-cellular interactions in the context of angiogenesis. To do this, we validate our spatio-temporal cellular model of angiogenesis against empirical data, and within this framework, focus on the effects of extracellular matrix topography on capillary sprout morphology and average extension speeds. We vary the density of the matrix fibers to simulate different tissue environments and to explore the possibility of manipulating the extracellular matrix to achieve pro- and anti-angiogenic effects. The model predicts specific ranges of matrix fiber densities that maximize sprout extension speed, induce branching, or that interrupt normal angiogenesis. We then explore matrix fiber alignment as a key factor contributing to peak sprout velocities, and in mediating cell shape and orientation. We also quantify the effects of proteolytic matrix degradation by the tip cell on sprout velocity and conjecture that degradation promotes sprout growth at high densities, but has an inhibitory effect at lower densities. Our results are discussed in the context of ECM targeted pro- and anti-angiogenic therapies that can be tested empirically.

Key words: angiogenesis; morphology; cell motility; chemotaxis; extracellular matrix; cellular Potts model

Introduction

The extracellular matrix (ECM) is a major component of the extravascular tissue region, or stroma, and plays a central role in morphogenesis, including embryogenesis (1), tissue repair and wound healing (2), new blood vessel growth (3), and cancer invasion (4). A large body of research is concentrated on understanding how cell-ECM interactions impact and regulate morphogenic processes. Results from such investigations illuminate the active role of the ECM in transmitting biochemical signals and mechanical forces that can mediate cell survival, phenotype, shape, and orientation. This area continues to be a target of intense investigation.

The ECM is a complex mesh-like molecular network largely composed of fibrous collagen proteins, elastin, adhesive proteins, such as fibronectin, and proteoglycans (5). Type I collagen (collagen) is the most abundant protein in the extracellular matrix (6). The collagen molecule is a triple helical protein approximately 300 nm long and 1.5 nm in diameter (6). Due to its molecular sequence, collagen molecules have a tendency to form covalent bonds with each other and self-assemble into larger fibrils (6, 7). Collagen fibrils also associate into larger bundles of matrix fibrils, referred to as fibers, that have been estimated to be between 100 and 1000 nm thick (8).

ECM mediated changes in cell phenotype

Cells are equipped with and can upregulate transmembrane receptors that enable them to receive signals from and interact with their environment. Integrins are one such receptor and are stimulated by the various proteins of the ECM (9, 10). Integrins are heterodimers composed of α and β subunits. Each subunit has a large extracellular domain, a transmembrane segment, and two smaller cytoplasmic tails (11). Integrin receptors mediate transmembrane signal transduction via "inside-out" signaling and "outside-in" signaling. Biochemical signals originating within the cell can affect integrin-ligand binding affinity (inside-out) and consequently modulate cellular adhesion to the matrix. For example, intracellular signaling and adaptor proteins, such as α-actinin, vinculin, and focal adhesion kinase ($pp125^{FAK}$), associate with the cytoplasmic integrin domain forming an integrin-activating complex, or focal adhesion complex (11, 12). This activating complex induces spatial changes in the cytoplasmic tails, which in turn, alters the configuration of the extracellular domain and the binding affinity of the integrin receptor. Endothelial cells attach directly to the collagen fibers in the ECM

through the $\alpha 1\beta 1$ and $\alpha 1\beta 2$ integrin receptors (7). Intracellular signaling pathways are then initiated that influence cell survival, growth, and that regulate the actin cytoskeleton necessary for cell motility (outside-in) (3, 13). Focal adhesion complexes form and bind directly to the cell's cytoskeleton (12). Once assembled, a focal adhesion anchors the cell to the ECM, which is used by the cell for movement. These focal adhesions are assembled and disassembled dynamically to facilitate cell migration. Migratory guidance via focal adhesion binding sites in the ECM is a phenomenon referred to as contact guidance and plays a key role in guiding new vessel growth (14). Contact guidance results in biased cellular motion in the direction of matrix fiber alignment. This differs from haptotaxis, which is another mechanism for directed cell motility whereby cells move in response to gradients of adhesion. The haptotactic response is to adhesive glycoproteins, such as fibronectin, found in the extracelluar matrix.

Experiments have linked the mechanical forces induced by cell attachment to the ECM via integrins to changes in a cell's internal molecular machinery (15). Such tension-dependent alterations affect signal transduction pathways, cellular biochemistry, and changes in the cytoskeleton (15). Experiments using human microvascular endothelial cells on substrates patterned with adhesive islands were performed to explore how the ECM influences cell shape and cellular function (13, 16). In these experiments, cell shape was regulated by controlling the size and number of adhesive islands. It was found that cells on adhesive islands allowing sufficient cell spreading successfully entered and progressed through their growth cycle. As the size of the adhesive islands was reduced, cell spreading was limited and the cells entered a program of apoptosis. Even in the presence of saturating concentrations of growth factor, loss of anchorage to the ECM resulted in cell cycle cessation and apoptosis. These studies reveal the important relationship between cell shape and function and the role of the ECM as a key mediator.

Mechanical properties of the ECM

How the physical properties of the ECM, such as density and stiffness, affect cell behavior has also been studied. Using endothelial cells on Matrigel^{TM}, increasing the stiffness of the gel or disrupting the organization of the cellular cytoskeleton inhibits the formation of vascular cell networks (17, 18). It has also been shown that matrices with lower fiber density transfer more strain to the cell (19). Cells respond to changes in force from alterations in the mechanical properties of the ECM, for example, by upregulating their

focal adhesions on stiffer substrates (20). For anchorage-dependent cells, including endothelial cells, increasing the stiffness of the ECM therefore results in increased cell traction and slower migration speeds (20). Moreover, experiments of endothelial cells cultured on collagen gels demonstrate that directional sprouting, known as branching, is induced by collagen matrix tension (21). Thus, via integrin receptors, the mechanical properties of the ECM influence cell-matrix interactions and modulate cell shape, cell migration speed, and the formation of vascular networks.

Understanding how individual cells interpret biochemical and mechanical signals from the ECM is only part of the whole picture. Morphogenic processes also require multicellular coordination. In addition to the guidance cues cells receive from the ECM, they also receive signals from each other. During new vessel growth, cells adhere to each other through cell-cell junctions, called cadherins, and in order to migrate, cells must coordinate integrin mediated focal adhesions with these cell-cell bonds. This process is referred to as collective or cluster migration (22). During collective migration, cell clusters often organize as 2D sheets (22). Cells also have the ability to condition the ECM for invasion by producing proteolytic enzymes which degrade specific ECM proteins (23). In addition, cells can synthesize ECM components, such as collagen and fibronectin (18, 24), and can further reorganize the ECM by the forces they exert on it during migration (17–19). In a study of cell-matrix strain transfer properties of 3D collagen tissue constructs under varied mechanical loading and collagen concentrations, collagen fibrils aligned in response to mechanical loading and cells reoriented with the direction of the applied load (19). Tractional forces exerted by vascular endothelial cells on Matrigel^{TM} caused cords or tracks of aligned fibers to be formed promoting cell elongation and motility (18). As endothelial cells restructure the ECM, they can also cause the release of angiogenic factors that were bound to the ECM (25–27). These newly liberated angiogenic factors are then available for endothelial cells to use to further coordinate their movement through the stroma (26, 27). Considerable attention has been given to the role of growth factors, such as vascular endothelial growth factor (VEGF), in endothelial cell migration, survival, and proliferation. However, as more experimental data is amassed, the ECM is emerging as the vital component to these morphogenic processes.

Experimental assays of angiogenesis are performed in a variety of *in vivo* animal models (28, 29) and *in vitro* matrix gels (13, 18, 30, 31) and the actual densities of these model extracellular matrices vary. Physiological

values for the volume fraction of collagen fibers in healthy tissues range from 0.026 in the myocardium, 0.142 in skeletal muscle, 0.293 in the corneal stroma, to 0.661 in the dermis (32). To aid our understanding of vessel growth in various tissues and to evaluate the efficacy of manipulating the extracellular matrix as a pro- and anti-angiogenic therapy, we focus our investigations on how the topography of the ECM influences, via cell-matrix adhesion, individual and collective cellular responses during early angiogenic sprout development.

In this work, we employ our cellular model of angiogenesis to investigate the effects of ECM topography on cell-matrix interactions during vascular morphogenesis. We show the dependence of sprout extension speed and morphology on matrix density, fiber network connectedness, and fiber orientation. Most notably, we observe that varying matrix fiber density effects a striking difference in the likelihood of capillary sprout branching, predicting an optimal density for capillary network formation and suggesting high fiber anisotropy as a mechanism for sprout branching. We also identify unique ranges of matrix density that promote sprout extension or that interrupt normal angiogenesis and show that maximal sprout extension speeds are achieved within a density range similar to the density of collagen found in the cornea. Finally, we quantify the effects of proteolytic matrix degradation by the tip cell on sprout velocity and conjecture that degradation promotes sprout growth at high densities, but has an inhibitory effect at lower densities.

This paper is organized in the following manner. First, we discuss several key improvements to our cellular model of angiogenesis (33) and validate this extended model against empirical measurements of sprout extension speeds *in vivo*. We then use our model to investigate the effect of ECM topography on vascular morphogenesis and focus on mechanisms controlling cell shape and orientation, sprout extension speeds, and sprout morphology. Based on our findings, we suggest and discuss several ECM targeted pro- and anti-angiogenesic therapies that can be tested empirically.

Cellular Model of Angiogenesis

We previously published a cell-based model of tumor-induced angiogenesis (33) that captures endothelial cell migration, growth, and division at the level of individual cells. That model also describes key cell-cell and

cell-matrix interactions, including intercellular adhesion, cellular adhesion to matrix components, and chemotaxis to simulate the early events in new capillary sprout formation. In the present study, we extend that model to incorporate additional mechanisms for cellular motility and sprout extension and use vascular morphogenesis as a framework to study how ECM topography influences intercellular and cell-matrix interactions.

Our vascular morphogenesis model uses a partial differential equation to describe the spatio-temporal dynamics of vascular endothelial growth factor (VEGF) coupled with a lattice-based cellular Potts model describing individual cellular interactions. At every time step, the discrete and continuous models feedback on each other and describe the time evolution of the extravascular tissue space and the developing sprout. The discrete model evolves by the Metropolis algorithm: the lattice updates are accepted probabilistically if the update reduces the total energy of the system. The energy, E, includes a term describing cell-cell and cell-matrix adhesion, a constraint for cellular growth, and an effective chemotaxis potential that is proportional to the local VEGF gradient, ΔV, and is given by:

$$E = \underbrace{\sum_{\text{sites}} J_{\tau,\tau'}\left(1-\delta_{\sigma,\sigma'}\right)}_{\text{adhesion}} + \underbrace{\sum_{\text{cells}} \gamma_{\tau}\ \left(a_{\sigma}-A_{\sigma}^{T}\right)^{2}}_{\text{growth}} + \underbrace{\sum_{\text{sites}} \chi_{\sigma}\Delta V}_{\text{chemotaxis}}\ . \qquad (1)$$

In the first term of Eq. 1, $J_{\tau,\tau'}$ represents the binding energy between model constituents. For example, $J_{\mathrm{e,e}}$ describes the relative strength of cell-cell adhesion that occurs via transmembrane cadherin proteins. Similarly, $J_{\mathrm{e,f}}$ is a measure of the binding affinity between an endothelial cell and a matrix fiber through cell surface integrin receptors. Each cell is associated with a unique identifying number, σ, and $\delta_{\sigma,\sigma'}$ is the Kronecker delta function. Thus $(1-\delta_{\sigma,\sigma'})$ ensures that the adhesive energy only accrues at cell surfaces. The second term describes the energy expenditure required for cell growth and deformation. a_{σ} denotes cell σ's current volume and A_{σ}^{T} is a specified "target" volume. For proliferating cells, the target volume is double the initial volume. In the third term, the parameter $\chi_{\sigma} < 0$ is the effective chemical potential and influences the strength of chemotaxis relative to other parameters in the model and $V = V(x, y, t)$ denotes the concentration of VEGF. A source of VEGF, S, is supplied to the stroma from the right hand boundary. A gradient of VEGF is established as VEGF diffuses through the stroma with diffusivity coefficient $D > 0$, decays at a constant rate $\lambda > 0$, and is taken up by endothelial cells, $B(x, y, V)$. The spatial profile of VEGF

satisfies a partial differential equation of the form:

$$\frac{\partial V}{\partial t} = D\nabla^2 V - \lambda V - B(x, y, V). \quad (2)$$

Initial and boundary conditions for VEGF are $V(x, y, 0) = 0$ and $V(0, y, t) = 0, V(l_1, y, t) = S, V(x, 0, t) = V(x, l_2, t)$. A complete description of this model, including a biochemical derivation of the function for endothelial cell binding and uptake of VEGF, has been previously published (33). The physical meanings of the symbols and their parameter values are listed in Table 1.

To more accurately capture the cell-cell and cell-matrix interactions that occur during morphogenesis, we have implemented several additional features to this model. The major improvement is the implementation of rear retraction, which refers to the ability of cells to release their trailing adhesive bonds with the extracellular matrix during migration. In moving multicellular clusters, rear retraction is a collective process that involves many cells simultaneously (22). Rear retraction is implemented in our model by allowing a lattice site that is occupied by an endothelial cell to be replaced by extracellular matrix components. This modification makes it possible for individual cells, as well as the entire sprout body, to migrate away from the parent vessel, making it necessary to consider cell recruitment from the parent vessel.

During the early stages of angiogenesis, cells are recruited from the parent vessel to facilitate sprout extension (34). Bautch et al. (35) measured the number and location of cell divisions that occur over 3.6 hours in *in vitro* vessels 8 days old (a detailed description of these experiments is provided in our discussion of model validation). They defined the sprout field as the area of the parent vessel wall that ultimately gives rise to the new sprout and the sprout itself. The sprout field was further broken down into regions based on distance from the parent vessel and was classified as distal, proximal, and nascent. They reported that 90% of all cell divisions occur in the parent vessel and the remaining 10% were located in the nascent area of the sprout field, at or near the base of the sprout. On average, total proliferation accounted for approximately 5 new cells in 3.6 hours, or 20 cells in 14 hours. This data suggests that there is significant and sufficient proliferation in the primary vessel to account for and facilitate *initial* sprout extension. This data does not suggest that proliferation in other areas of the sprout field does not occur at other times. In fact, it has been established that a new sprout can migrate only a finite distance into the stroma without prolifera-

tion and that proliferation is necessary for continued sprout extension (36). We model sprout extension through a cell-cell adhesion dependent recruitment of additional endothelial cells from the parent vessel. As an endothelial cell at the base of the sprout moves into the stroma, it drags a cell from the parent vessel along with it. We assume, based on the data presented in (35), that there is sufficient proliferation in the parent vessel to provide the additional cells required for initial sprout extension while maintaining the physical integrity of the parent vessel.

As in our previous model, once a cell senses a threshold concentration of VEGF, given by v_a, it becomes activated. We recognize that cells have distinct phenotypes that dictate their predominate behavior. We distinguish between tip cells, cells that are proliferating, and stalk cells. As before, tip cells are functionally specialized cells that extend filopodia and concentrate their internal cellular machinery to promote motility (37). Tip cells are highly migratory cells and do not proliferate (35, 37). The remainder of the cells are designated as stalk cells and use adhesive binding to and retraction from the matrix fibers for support and to facilitate cohort migration. Stalk cells can also sense chemical gradients although they exhibit a weaker chemotactic, or motile, response than the specialized tip cell. Proliferating cells are located behind the sprout tip (35, 37) and increase in size as they move through an 18 hour cell cycle clock in preparation for cell division (38). Cells that are proliferating can still migrate (35); it is only during the final stage of the cell cycle that endothelial cells stop moving and round up for mitosis (personal communication with C. Little). As we assume that the presence of VEGF increases cell survivability, we do not model endothelial cell apoptosis.

Cells must simultaneously negotiate multiple forces, namely, intercellular adhesion, chemotactic forces, and tractional forces as cells adhere to matrix fibers. To do so, cells deform their shape and dynamically regulate adhesive bonds. However, in the model, it is also possible that in concert these forces may cause a cell to be pulled or split in two. To balance these external forces, we introduce a continuity constraint that preserves the physical integrity of each individual cell. This constraint expresses that it is energetically expensive to compromise the physical integrity of a cell and is incorporated into the equation for total energy (Eq. 1) by including a term of the form:

$$E_{\text{continuity}} = \sum_{\text{cells}} \alpha \left(1 - \delta_{a_\sigma, a'_\sigma}\right), \tag{3}$$

where α is an effective *intra*cellular adhesion energy, a_σ represents the current size of the endothelial cell with unique identifying number σ, and a'_σ is a breadth first search count of the number of continuous lattice sites occupied by that endothelial cell. Thus, $a'_\sigma \neq a_\sigma$ signals that the physical integrity of the cell has been compromised and a penalty to total energy is incurred.

As described in our previous work (33), we model the mesh-like anisotropic structure of the extracellular matrix by randomly distributing 1.1 μm thick bundles of individual collagen fibrils at random discrete orientations between -90 and 90 degrees. Model matrix fibers comprise approximately 40% of the total stroma and the distribution of the ECM is inhomogeneous, with regions of varying densities. To relate the density of this model fibrillar matrix to physiological values, we measure matrix fiber density as the ratio of the interstitium occupied by matrix molecules to total tissue space, $0 \leq \rho \leq 1$, and compare it to measured values of the volume fraction of collagen fibers in healthy tissues (32).

Parameter Calibration

A list of values for the model parameters is provided in Table 1, including references. Parameters are taken from experimental data whenever possible. If no reference is given, the parameter is a relative value chosen to emulate the physical properties and behaviors of cells. The membrane elasticities, γ_τ, are chosen to reflect the relative compressibility of the cell, fiber, or of interstitial fluid. The chemotactic potential, χ_σ, is chosen so that its contribution to the change in total energy is the same order of magnitude as the contribution from adhesion or growth. The difference between the concentration of VEGF at two adjacent lattice sites is on the order of 10^{-4}. To balance adhesion and growth, χ_σ must be on the order of 10^6. We calibrated this parameter to maximize sprout extension speeds while maintaining the physical integrity of the cells. By equating the time it takes an endothelial cell to divide during the simulation with the endothelial cell cycle duration of 18 hours, we convert Monte Carlo steps to real time units. In the simulations reported in this paper, 1 Monte Carlo step is equivalent to 1 minute.

Results

Model Validation

The canonical benchmark for validating models of tumor-induced angiogenesis is the rabbit cornea assay (28, 45). In this *in vivo* model, tumor implants were placed in a corneal pocket approximately $1-2$ mm from the limbus. New vessel growth was measured with an ocular micrometer at 10x, which has a measurement error of $\pm$ 0.1 mm or 100 μm. Initially, growth was linear and sprout extension speeds were estimated at a rate of 0.5 mm/day, or 20.8 ± 4.2 μm/hr. Sprouts then progressed at average speeds estimated to be between $0.25-0.50$ mm/day, or $10.4-20.8 \pm 4.2$ μm/hr. More recent measurements of sprout extension speeds during angiogenesis were reported in Bautch et al. (35). In this study, embryonic stem cells containing an enhanced green fluorescent protein were differentiated *in vitro* to form primitive vessels. Day 8 cell cultures were imaged within an $\sim$160 μm^2 area at 1 minute intervals for 10 hours and they observed sprouting angiogenesis over this period. The average extension speeds for newly formed sprouts were 14 μm/hr and ranged from 5 to 27 μm/hr. Growth factor was present and was qualitatively characterized as providing a diffuse, or shallow, gradient. No quantitative data pertaining to growth factor gradients or the effect of chemotaxis during vessel growth were reported (35).

We use the above experimental models and reported extension speeds as a close approximation to our model of *in vivo* angiogenesis for quantitative comparison and validation. We simulate new sprout formation originating from a parent vessel in the presence of a diffusible VEGF field, which creates a shallow VEGF gradient. We measure average extension speeds over a 14 hour period in a domain 100 μm by 160 μm. As was done in Bautch et al. (35), we calculate average sprout velocities as total sprout displacement in time and measure sprout displacement as the distance from the base of the new sprout to the sprout tip. Figure 1 shows average sprout extension speed over time for our simulated sprouts. Reported speeds are an average of 10 independent simulations using the same initial VEGF profile and parameter set as given in Table 1. Error bars represent the standard error from the mean. The average extension speeds of our simulated sprouts are within the ranges of average sprout speeds measured by both Bautch et al. (35) and Gimbrone et al. (45).

Figure 1 also reveals that average sprout extension speed changes as a func-

tion of time. Within the first two hours, speeds average $\sim 30\mu$m/hr and the new sprout consists of only $1-2$ endothelial cells. At two hours, sprouts contain an average of 3 cells and at 4 hours, there are a total of $5-6$ cells. Over time, as cells are added to the sprout, cell-cell adhesion and cumulative cellular adhesion to the extracelluar matrix start to play a role and sprout extension speeds slow. The inset in Figure 1 shows the geometry of the computational domain and simulated sprout development. Endothelial cells (red) have migrated into the domain from a parent blood vessel (left boundary); a source of growth factor is available and diffuses from the right boundary. The space between represents the stroma and is composed of extracellular matrix fibers (green) and interstitial fluid (blue). On average, our simulated sprouts migrate 160 μm and reach the domain boundary in approximately 15.6 hours, before any cells in our model have had time to proliferate. We do not expect to see proliferation in the new sprout because the simulation duration is less than the 18 hour cell cycle and we set the cell cycle clock to zero for newly recruited cells to simulate the very onset of angiogenesis. In our simulations, sprout extension is facilitated by cell recruitment from the parent vessel. Between 15 and 20 cells are typically recruited, which agrees with the number of cells we estimate would be available for recruitment based on parent vessel cell proliferation reported by Bautch et al. (35). In those experiments (35), proliferation in the parent vessel was measured for day 8 sprouts, which likely had cells at various stages in their cell cycles. Proliferation in the new sprout is another mechanism for sprout extension. Thus, we consider the possibility that cells recruited from the parent vessel may be in different stages of their cell cycles by initializing the cell cycle clock of each recruited cell at randomly generated times. We observed no differences in extension speeds, sprout morphology, or the number of cells recruited as a result of the assumption made for cell cycle initialization ($t = 0$ or t random). This suggests that, in our model, stalk cell proliferation and cell recruitment from the parent vessel are complementary mechanisms for sprout extension.

By adjusting key model parameters, we are able to simulate various morphogenic phenomena. For instance, by increasing the chemotactic sensitivity of cells in the sprout stalk and decreasing the parameter controlling cellular adhesion to the matrix, J_{em}, we are able to capture stalk cell migration and translocation along the side of a developing sprout (supplemental movie S1). This phenomena, where stalk cells weaken their adhesive bonds to the extracellular matrix and instead use cell-cell adhesion to facilitate rapid migration, frequently occurs in embryogenesis (personal communica-

tion with C. Little) and is described as preferential migration to stretched cells (46). Figure 2 shows the morphology for one particular set of parameter values corresponding to weaker cell-cell and cell-matrix adhesion and stronger chemotaxis. Here the average extension speed at 14 hours is 6.8 μm/hr, fewer cells are recruited from the parent vessel, and cells elongate to approximately 40 μm in length. This length scale is consistent with experimental measurements of endothelial cell elongation (47). Figure 3a shows images from experiments using human fibroblasts stained for actin (e) and tubulin (f) on micro-machined grooved substratum (55). These experiments demonstrate that cells alter their shape, orientation, and polarity to align with the direction of the grooves (double-headed arrow), exhibiting topographic, or contact, guidance. Figure 3b is a simulation designed to mimic these experiments by isolating the cellular response to topographical guidance on similarly patterned substratum. In this simulation, there is no chemotaxis and no cell-cell contact; cells respond only to topographical cues in the extracellular matrix. Simulated cells alter their shape and orient in the direction of the matrix fibers. Figure 3b bears a striking resemblance to the cell shapes captured in Figure 3a. We are also able to simulate interstitial invasion/migration by a single cell by turning off proliferation and cell recruitment but leaving all other parameters unchanged (supplemental movie S2). This is especially relevant in the context of fibroblast recruitment during wound healing and tumor cell invasion (e.g., glioblastoma, the most malignant form of brain cancer (48)), where understanding cell-matrix interactions and directed motility are critical mechanisms for highly motile or invasive cell phenotypes.

Model predicts ranges of matrix fiber density that may inhibit angiogenesis *in vivo*

We designed a set of numerical experiments allowing us to observe the onset of angiogenesis in extravascular environments of varying matrix fiber density. We consider matrix fiber densities given as a fraction of the total interstitial area, ρ, corresponding to physiological quantities of collagen ranging from 0.0-0.53 g/ml. As a measure of matrix orientation equivalency, the total fiber orientation in both the x and the y direction was calculated as we increased the matrix density. It was confirmed that the total x and total y fiber orientation did not change with changes in total matrix density. Besides varying the matrix density, all other parameters were held fixed. All simulations lasted the same duration corresponding to approximately 14 hours.

The average rate at which the sprout grows and migrates, or its average extension speed, is calculated as the total tip cell displacement in time. Average extension speeds in microns per hour (μm/hr) versus matrix fiber density are graphed in Figure 4a at various times (2, 5, 10, 14 hours) during sprout development. We identified qualitative measures to describe and differentiate between various capillary sprout morphologies, such as the thickness of the sprout, its tortuosity, and whether sprout branching or anastomosis occurred. Following Bautch et al., we define a sprout branch as one or more cells that extend, or bud, from the primary sprout body at least 10 μm (35). Capillary sprout thickness and the incidence of branching versus the fraction of matrix fibers present in the stroma are reported in Figure 4b.

Figure 4 demonstrates that the density of the matrix impacts the average rate at which a capillary sprout extends and the resulting sprout morphology. At very low ratios (< 0.10), the matrix fibers are sparse, disconnected filaments (Figure 5a). In a study of vasculogenesis using endothelial cells plated on varying densities of collagen or fibronectin, cell attachment, spreading, and tube formation were maximal on dishes of intermediate density, reported to be $100-500$ ng/cm^2 (49). Whereas, at matrix densities below 100 ng/cm^2, cells detached from the substrate and lost their viability (49). Our model predicts a coincident interruption of normal angiogenesis and loss of sprout viability at very low matrix fiber densities (< 0.10). Matrices with lower fibril density transfer more strain to the cell (19). Effects of the high transfer of strain can be seen in Figure 5a, which shows severe cell elongation at $\rho = 0.05$. Compare with the inset in Figure 1, which is an identical simulation except for an increase in the ECM density ($\rho = 0.4$). This higher density matrix transfers less strain to the cells and consequently cells are rounder. Additionally, because there are more focal adhesion sites in this denser matrix, cells are able to maintain their cell-cell contacts and develop as a cohesive body. We do not report migration speeds for $\rho < 0.1$ or $\rho > 0.8$ because sprouts show developmental defects, that is, cells are severely elongated or detach from each other and do not form a cohesive sprout body.

For $0.15 \leq \rho \leq 0.25$, the fiber network is stiff and highly inhomogeneous, and a large amount of strain gets transferred to the cells. As a result we see an increase in cell spreading and a thickening of the new sprout as compared to those morphologies seen for $\rho < 0.15$ (compare Figures 5a and 5b). These values of ρ correspond to the same fraction of collagen present in subcutaneous tissue ($\rho = 0.212$) and some skeletal muscle ($\rho = 0.09 - 0.189$) (32).

Remarkably, we see a distinct range of densities, $0.20 - 0.30$, where new buds develop from the main sprout body and branches begin to form (see arrow in Figure 5b). This suggests that mechanical mechanisms, such as a high degree of fiber anisotropy and matrix stiffness, may promote branching. This is consistent with reports that collagen matrix tension induces directional sprouting in endothelial cells (21). Figure 4b quantifies the incidence of branching for and the average thickness of sprouts developing in different matrix densities. At all densities, sprout thickness was within the normal physiological range of $1-2$ cells wide. Figure 5c shows sprout development on a matrix where $\rho = 0.25$. Morphologies that could be interpreted as lumen formation or anastomosis (loop formation), are evident, and are only seen at this density. Figure 4a reveals a clear range of matrix density that encourages sprout migration and results in faster average speeds, and ranges that present a physical barrier to migration and inhibit sprout growth and results in slower extension speeds. The peak in the graph at $\rho = 0.35$ indicates that sprout extension speeds are fastest at intermediate densities between $0.3 \leq \rho \leq 0.4$ and suggests an optimal matrix density for promoting angiogenesis. For comparison, this range of matrix density is near the physiological fraction of collagen fibers found in the cornea (32). A possible mechanistic explanation for the existence of a peak extension velocity is that the mechanical properties of the ECM around $\rho = 0.35$ provide contact guidance cues that are aligned with chemotactic forces. Referring again to Figure 4a, we see that peak migration speeds are prominent at 2 hours, but are still evident, although to a lesser extent, at 10 and 14 hours. Thus, these results do not depend on time. Our finding that maximum migration speeds depend on matrix density is supported by empirical measurements of endothelial cell migration speeds on various fibronectin concentrations (0.5, 1, 5, 20, 40 μg/cm^2) demonstrating peak migration speeds at intermediate concentrations (5 μg/cm^2) (50).

As matrix density increases, the network of fibers is extensive and the matrix becomes more flexible and malleable (18). The higher fiber density translates into greater matrix homogeneity and a loss of strong guidance cues from fiber anisotropy. Chemotaxis then plays a stronger role in sprout guidance producing linear sprouts (Figure 5d). Consequently, we do not observe any branching at densities above $\rho = 0.35$. At a fiber density of $\rho = 0.70$, the matrix is less rigid and less tension is transferred to the cells. Cells experiencing less tension are rounder. Sprout formation on matrix that is more malleable results in a wider and slower sprout (Figure 5e). Above $\rho = 0.75$, very high matrix densities actually establish a physical barrier to

migration and we see a corresponding reduction in sprout extension speed due to increased focal adhesion contacts and strong tractional forces. Figure 5f shows complete inhibition of angiogenesis at $\rho = 0.99$ as tractional forces dominate chemotactic incentives.

Network connectedness and matrix fiber alignment influence sprout extension speeds

Based on our earlier observations, the density of ECM fibers affects capillary sprout migration speeds. As matrix density is increased, a connected fibrous network develops which could be a mechanism for differences in observed average speeds. We hypothesized that peak extension speeds occur when the mechanical properties of the ECM provide contact guidance cues that are aligned with the chemotactic forces. To examine the effects of matrix fiber alignment on average rates of capillary sprout elongation, we devise another set of numerical experiments. If matrix fiber alignment plays a prominent role in sprout migration, we would expect more rapid rates of sprout elongation when matrix fibers are aligned with VEGF gradients than when matrix fibers are aligned perpendicular to the gradient. We look at three specific cases: matrix fibers aligned perpendicular to VEGF gradients, matrix fibers aligned with the VEGF gradient, and a combination of horizontal and vertical fibers only. We compare these test cases with the baseline simulations of sprout development on matrices of random fiber orientation. We distinguish and refer to these three cases by the angle that is formed between the fiber axis and the axis of the VEGF gradient. For instance, 0° denotes a matrix with fibers aligned with the gradient and 90° identifies a matrix of fibers perpendicular to the VEGF gradient. These numerical experiments represent a simplified replica of the matrix fiber restructuring and fiber alignment that occurs as a result of the tractional forces exerted by endothelial cells during migration (18, 21). All matrices have the same matrix fiber density.

As matrix fiber density increases, both the number of focal adhesion binding sites available in the ECM and the connectivity of the fiber network increase. As a measure of connectivity, we consider the network connected if there exists a continuous path along matrix fibers from the parent vessel to the source of chemoattractant. As the density of matrix fibers increases, there will be a density that guarantees network connectedness. This threshold density is known as a percolation threshold. Our model fiber networks are constructed by randomly placing fibers at randomly selected but discrete orientations: 0°, $\pm 30^\circ$, $\pm 45^\circ$, $\pm 60^\circ$, and 90°. Consequently, our fiber net-

work most closely approximates a triangular lattice. We estimate that the percolation threshold in our fiber networks occurs between $\rho = 0.30 - 0.35$. Recall that we define matrix density, ρ, as the fraction of total tissue space occupied by collagen fibers. This can be interpreted as the probability that a matrix fiber occupies, that is, a bond exists between, two neighboring lattice sites. The bond percolation thresholds depend on lattice geometry and is 0.35 for a two-dimensional triangular lattice (51). The matrix percolation threshold observed in our random matrices corresponds to the bond percolation threshold for a 2D triangular lattice. Interestingly, this percolation threshold is coincident with the density at which our model predicts maximum sprout elongation rates. This is because, at the percolation threshold, "tracks" of matrix form and provide strong contact guidance cues to the developing sprout. This finding suggests that capillary sprout extension rates are positively related to the connectedness of the network.

Figure 6a−c reports the average extension speed of new sprouts forming on these restructured matrices for $\rho = \{0.2, 0.4, 0.6\}$ respectively. The baseline for comparison is the average extension speed for sprouts formed on matrices with random fiber alignment and is plotted as a solid black line in each plot. At $\rho = 0.2$, there are fewer focal adhesion sites in the ECM and the matrix fibers do not form a well connected network. Consequently, at this density, matrix fiber alignment does not have a strong effect on sprout extension speeds. At $\rho = 0.4$ and $\rho = 0.6$, sprouts achieve statistically significant higher average extension speeds when the fibers are aligned with the VEGF gradient (0°) than when fibers are aligned perpendicular to the chemogradient (90°). The slowest speeds occur on matrices with fibers aligned perpendicular to the VEGF gradient. Interestingly, sprout extension speeds on a matrix composed of randomly oriented fibers are almost as fast as those observed on matrices aligned with the gradient (0°). The reason for this is clear if we consider the vector describing the net force, or resultant force, due to fiber orientation. For 0° and 90° matrices, the resultant forces are in the 0° and 90° directions respectively. For matrices composed of fibers aligned in both 0° and ±90°, the resultant force is at a ±45° angle. This explains why 0° matrices facilitate the fastest extension speeds and 90° matrices the slowest. For matrices with a random fiber orientation, the resultant force is at a ±11° angle. Since the resultant force for random matrices is approximately aligned with the gradient (±11°), this accounts for our observation that the corresponding extension speeds are close to those speeds recorded on 0° matrices. In these computer generated matrices, the fibers are oriented at discrete angles and thus have a net orien-

tation. Biologically, we are not limited to these discrete angles. Depending on the tissue type, fibers may already be aligned, for instance in muscle, or the tissue may be isotropic and lack any structural orientation. Compared to $\rho = \{0.2, 0.6\}$, the effect of matrix fiber alignment is greatest at $\rho = 0.4$. This is because at $\rho = 0.4$, the fiber network is well connected and provides adequate focal adhesion sites but still retains sufficient anisotropy such that strong guidance cues are transferred through fiber orientation. At higher densities ($\rho = 0.6$), even though there are ample focal adhesion binding sites, the matrix is more homogeneous, matrix "tracks" become less evident, and strong migratory cues from matrix anisotropies are lost. Consequently, the effect of matrix alignment on average extension speed decreases. These results support our hypothesis that when mechanical or contact guidance cues from the ECM are aligned with the direction of chemotaxis, these forces cooperate and promote sprout extension.

Cell shape and orientation are linked to matrix fiber alignment

In light of the above results, we constructed patterned matrix topographies to look at the effect of unambiguous contact guidance cues on cell shape, orientation, and sprout morphology. In these numerical experiments, instead of distributing fiber bundles, we engineered matrix cord patterns that vary in width and orientation. As a baseline, we augmented a matrix of randomly distributed fibers with horizontal cords 7.2 μm thick (Figure 7a). Figure 7b−e shows sprout development on matrix cords 7.2 μm thick aligned horizontally, horizontal cords 2.2 μm thick, vertical cords 2.2 μm thick, and crosshatched cords. Horizontal cords are aligned with the VEGF gradient (0°); vertical cords are perpendicular to the gradient (90°); crosshatched cords form a $\pm 45°$ angle with the gradient. Except for the topography of the ECM, all other model parameters are unchanged.

We found a strong correspondence between fiber alignment and cell shape and orientation. We define cell orientation as the axis of elongation. In Figure 7a, the density of ambient fibers is great enough to form a well connected mesh and facilitate migration, whereas the higher density matrix cords present a physical barrier that requires more energy to overcome. The anisotropy of the fiber mesh promotes variable cell shapes with no obvious cell orientation. In contrast, in the absence of an ambient fiber mesh, cells quickly adhere to the matrix cords (Figure 7b). Cells orient and elongate in the direction of the horizontal cords. Figure 7c shows the result of reducing cord thickness from 7.2 to 2.2 μm (roughly 1/2 cell diameter). Cells dramat-

ically elongate and orient in the direction of the VEGF gradient. Compare these two cases to Figure 7a and notice that thinner more linear sprouts develop when strong and unambiguous contact guidance cues are aligned in the direction of chemotaxis. Next we examine the effects of matrix cords aligned perpendicular to the gradient. The results are shown in Figure 7d. In this case, although the sprout migrates toward higher concentrations of VEGF, cells elongate and are clearly oriented in the direction of the matrix cords, perpendicular to the gradient. Figure 7e depicts sprout formation on crosshatched matrix topography. Again, cells orient in the direction of the matrix cords, here at $\pm 45^\circ$ angles with respect to the gradient. The resulting morphology is a sprout approximately 2 cell diameters thick, notably thicker than the sprouts that develop with strong contact guidance cues aligned in the direction of chemotaxis (Figure 7b,c). Fiber orientation also modulates cell recruitment. When cells elongate and orient in the direction of the VEGF gradient, fewer cells are required from the parent vessel and sprout extension is largely due to cell elongation. Compare Figure 7: (a) with no obvious cell orientation 15 cells are recruited, (b) 11 cells are recruited when cells are oriented in the direction of the VEGF gradient, (c) only 3 cells are recruited when cells dramatically elongate, (d) 19 cells are needed when cell orientation is perpendicular to the chemoattractant gradient, and (e) 19 cells are recruited when cells orient at $\pm 45^\circ$ with respect to the gradient. These results demonstrate the important role of contact guidance and tissue structure in determining cell shape and orientation.

Changes in average extension rates due to tip cell matrix degradation varies as a function of ECM density

During angiogenesis, endothelial cells not only realign matrix fibers, but they also secrete matrix degrading proteases that break down extracellular matrix proteins and facilitate sprout migration through the stroma (34). To study the effect of matrix degradation on sprout development, we implement matrix degradation by allowing the tip cell to degrade $\sim 0.3\ \mu\text{m}^2$ of matrix each minute. We choose this rate of degradation based on the fact that focal adhesions are estimated to be $0.25\ \mu\text{m}^2$ (7). Average sprout extension speeds are recorded and compared with the average extension speeds without matrix degradation for different matrix densities. Figure 8 graphically represents average extension rate pairs for sprouts forming with and without matrix fiber degradation at $\rho = \{0.2, 0.4, 0.7, 0.975\}$ and shows that the effect of matrix degradation depends on matrix density. At $\rho = 0.7$ and $\rho = 0.975$, matrix degradation results in approximately a 37% increase in

average sprout extension speeds at hour 14. As matrix fibers are degraded, fewer cell-matrix adhesion sites are bound and therefore cellular attachment is reduced resulting in increased motility. At a matrix density of $\rho = 0.4$, tip cell matrix degradation only seems to have a significant influence on extension speed at earlier times ($0-5$ hours). This suggests that the increase in motility due to a loss of bound focal adhesion sites is limited. On more sparse matrices, $\rho = 0.2$, matrix degradation actually slows sprout extension. While this may seem counterintuitive, it is expected that at lower densities, reducing fiber density reduces the effectiveness of the ECM to provide a cellular support system that is necessary for normal sprout migration and formation. Thus, depending on the density of the matrix, matrix degradation may result in faster or slower extension speeds. This is consistent with our finding that sprout extension speeds vary as a function of matrix density (Figure 4a). In fact, at $\rho = 0.975$, the initial cell is not able to penetrate the stroma and angiogenesis is completely inhibited. However, in otherwise identical simulations, when the tip cell actively degrades the matrix fibers, the tip cell carves out a path through the ECM and a sprout is able to form (Figure 9a). Figure 8 also shows that for $\rho = 0.7$, tip cell matrix degradation has the greatest effect after 10 hours.

In our model, no branching is observed at matrix fiber densities above $\rho = 0.35$. Figure 9b shows the progress of sprout development at 14 hours with ECM degradation at $\rho = 0.4$. A new sprout has branched from the primary sprout body, an event that emerges only as a result of featured cellular and molecular level dynamics; no rule specifically incorporating branching is imposed. Tip cell degradation reduces ECM density and sets up very high local anisotropies in the matrix fiber structure, providing strong contact guidance cues to the developing sprout. This result provides additional support for our hypothesis that high matrix anisotropies created by tip cell degradation may be a mechanism for sprout branching.

Sensitivity Analysis

To ascertain the variability or sensitivity of our results to the choice of parameters, holding all other parameters fixed as listed in Table 1, we vary one parameter at a time and record our observations. We look at sprout development for various J_{ee}. Decreasing J_{ee} is equivalent to increasing the strength of the bond between endothelial cells and the cells move to increase their cell-cell contact area. For $J_{\text{ee}} \leq 10$ cell shapes are grossly contorted and unrealistic. As J_{ee} increases, cell-cell adhesion weakens. Cells move to

reduce their surface area contact with each other and are generally rounder. For $J_{\mathrm{ee}} \geq 50$, cell-cell adhesion becomes too weak relative to the chemotactic forces acting on the cell and the tip cell migrates away from the main sprout. We next consider J_{em}. Similarly, lower values of J_{em} correspond to stronger cell-matrix binding energies. For $J_{\mathrm{em}} \leq 46$, cell shapes are abnormally distorted to increase the contact area between the matrix fibers and the cell membrane. At $J_{\mathrm{em}} = 56$, a relatively strong cell-matrix adhesion bond, sprout morphology is noticeably thicker and more tortuous. Intermediate values ($66 \leq J_{\mathrm{em}} \leq 76$) provide a good balance between contact guidance and release of focal adhesion bonds and sprout morphologies and extension speeds are relatively insensitive to parameter variability within this range. Above $J_{\mathrm{em}} = 76$, contact guidance is weak. A value of $J_{\mathrm{em}} = 200$ is equivalent to inhibiting cell-matrix adhesion, for instance by blocking integrin receptors, and consequently, endothelial cells do not adhere to matrix fibers at all and are unable to migrate, even in the presence of chemotatic incentives. Chemotaxis is then the dominant force governing sprout guidance and more linear sprouts develop. There is no statistically significant change in average extension speeds as J_{em} varies within these ranges. The results are insensitive to the binding energies between matrix fibers, J_{mm}, or between interstitial fluid molecules, J_{ss}. The results also do not depend on the compressibility properties of the matrix fibers or interstitial fluid, $\gamma_{\mathrm{m,f}}$, since the total mass of these ECM components are conserved. We vary γ_{e} between 0.3 and 3. Decreasing γ_{e} makes it easier for the cells to deviate from their target volume. Therefore at $\gamma_{\mathrm{e}} = 0.3$, the cells are larger overall and consequently fewer cells are recruited from the parent vessel. Average extension speeds are not affected. This highlights that cell growth is another mechanism for sprout extension. Increasing γ_{e} produces smaller cells, and consequently, more are recruited. At $\gamma_{\mathrm{e}} = 3$, the tip cell migrates away from the main body of the sprout. This is because of the chemotactic sensitivity differential between the tip cell and the stalk cells. The relative pressure on a cell to maintain its target volume is greater than the chemotactic forces acting on the stalk cells, but not greater than the chemotactic incentives for the tip cell. Thus the tip cell detaches. Figure 10 shows how the average extension speed of a sprout varies with increasing χ. Average speeds are calculated at 14 hours. Above $\chi = 1.6 \cdot 10^6$, the physical integrity of individual endothelial cells is compromised and the cells dissociate due to the relatively strong chemotactic forces. Below $\chi = 1 \cdot 10^4$, chemotactic forces provide insufficient migratory cues relative to the adhesion energies and growth constraint and the initial cell does not migrate into the stroma. At intermediate values, sprouts migrate faster with increasing χ, but sprout

morphologies are unaffected. The parameter kT, where k is the Boltzmann constant and T is the effective temperature that corresponds to the amplitude of cell membrane fluctuations, is varied to look at the effect of changes in the probability that energetically unfavorable events occur. Increasing kT effects faster average sprout extension speeds, but no noticeable changes in cell shape, the number of cells recruited, or sprout morphology.

Discussion

The extracellular matrix has attracted a great deal of attention from researchers and experimentalists because of its vital role as a modulator of morphogenic processes. Identifying and elucidating the mechanisms through which the ECM contributes to changes in cell shape and function is of critical importance to many morphogenic events, including angiogenesis, wound healing, embryogenesis, and tumor invasion. We use a cell-based model of angiogenesis as a framework to explore the effects of ECM topography on cell-cell and cell-matrix dynamics. This type of modeling approach captures the precise morphology of the cells and of emergent multi-cellular structures and allows a quantitative description of physical characteristics, such as cell shape and orientation and sprout thickness. By adjusting key parameters in our model, we capture a frequent dynamic in embryogenesis whereby cells use cell-cell adhesion to rapidly traverse along the sprout, single cell migration as seen in fibroblasts during wound healing, and are able to simulate different cell shapes. Our results indicate that the density or connectedness of the matrix, local proteolytic matrix degradation, and fiber alignment affect extension speeds and we record peak migration speeds in tissues that have a similar collagen content to that seen in the cornea. We observe density dependent pro- and anti-angiogenic effects and propose that high matrix fiber anisotropy provides strong contact guidance cues and is a mechanism for initiating sprout branching. Finally, we provide strong evidence that contact guidance influences cell orientation by examining sprout development on engineered matrix patterns.

During morphogenesis, cells actively restructure and condition the extracellular matrix for migration through proteolytic degradation and fiber reorganization and alignment (14). Our studies indicate that contact guidance cues are mediated by changes in matrix fiber density and isotropy, network connectedness, and fiber orientation and collectively support the hypothesis that contact guidance cues play a major role in determining sprout mor-

phology and the average rate of capillary sprout extension. Our results strongly suggest that the contact guidance cues established through high matrix fiber inhomogeneity in the stroma may be a mechanism for sprout branching. Applying our results in the context of tumor-induced angiogenesis, local changes in ECM density that create matrix anisotropies in concert with fiber alignment, may contribute to the accelerated extension speeds reported as sprouts approach the tumor. In addition, fiber density is not constant in the extratumoral environment. The density of the extracellular matrix is lower near the tumor due to the secretion of matrix degrading proteases by tumor cells. If these lower regions of matrix density are within the range we predict to be conducive to branching, this could help explain why an increase in branching, known as the brush border effect, is seen *in vivo* as sprouts get close to the tumor. It is worth pointing out that at a distance of 100 μm from a tumor 1mm in diameter, we specify a linear source of VEGF. This choice ensures little or no gradient in the transverse or y−direction and allows us to attribute lateral cell and sprout movement to the mechanical effects of the matrix. However, different spatial profiles of VEGF, for example a parabolic source or local sinks and sources of VEGF in the ECM, could also contribute to branching and varied morphological patterns. The effect of different VEGF profiles on angiogenesis has been theoretically modeled by Anderson and Chaplain (52).

Clinical Implications: ECM Targeted Angiogenic Therapies

Increased understanding leading to the ability to control angiogenesis *in vivo* has serious clinical implications. Angiogenesis is a crucial event to many physiological processes. Embryonic development and endometrium vascularization, arteriogenesis resulting from ischemia and vessel occlusion, wound healing and tissue repair are all homeostatic processes that require new vessel growth for normal function. However, angiogenesis can also lead to pathological conditions. Tumor angiogenesis, proliferative diabetic retinopathy and macular degeneration, psoriasis and rheumatoid arthritis occur when angiogenesis is unhalted (53). On the other hand, insufficient vessel growth can lead to heart attack, stroke, and impaired ulcer and wound healing. Existing angiogenic therapies can be broadly categorized as (1) those that target growth factors or growth factor cell receptors that stimulate vessel growth, (2) those that block cell invasion into the stroma, and (3) those that directly induce endothelial cell apoptosis. Because of its established prominence in both homeostatic and aberrant angiogenesis, VEGF and its receptors are prime therapeutic targets. VEGF neutralizing antibodies, sol-

uble VEGF receptors, and receptor tyrosine kinase inhibitors are examples of therapies currently being utilized or that are undergoing clinical trials (54). One problem in targeting growth factors as therapeutic targets is that they are often constitutively expressed *in vivo* and can be proteolytically released. Thus tight control is, in practice, hard to maintain.

The ECM and cell-matrix associations also provide promising possibilities for angiotherapy, but have only more recently received attention as targets and are in less advanced stages of clinical development. Consequently, modeling and simulation have the potential to contribute to and propel further advancement. Current therapeutic interventions aimed at cell-matrix interactions during angiogenesis focus on tissue inhibitors of metalloproteinases (TIMPs) and on integrin-mediated cellular adhesion (53). Blocking proteolysis is intended to inhibit cellular migration into the stroma and to prohibit MMP-dependent release and activation of ECM sequestered angiogenic factors. The $\alpha v\beta 3$ integrin receptor is significantly upregulated in angiogenic vessels when compared to mature vessels (53) making this receptor a logical therapeutic choice.

Using our model, we regulate cell-matrix binding affinity (J_{em}) and control the number of focal adhesion binding sites available in the ECM (density modulation) to test the efficacy of integrin specific anti-angiogenic therapies. Setting $J_{\mathrm{em}} = 200$ is equivalent to blocking integrin receptors. Our simulations show that decreasing the binding affinity of integrin receptors prevents endothelial cells from adhering to matrix fibers and cells are unable to migrate even in the presence of chemotatic incentives. We also show that cellular motility is inhibited at high matrix densities due to the greater number of focal adhesion binding sites available. Our simulations suggest that regulating the affinity or number of cell-matrix focal adhesion sites either biochemically or mechanically produces anti-angiogenic effects. In addition, our results indicate that regulating the cellular production of matrix degrading proteases can shift sprout velocity curves for the purpose of promoting or inhibiting angiogenesis. We show that at low matrix densities ($\rho \leq 0.25$), matrix degradation has anti-angiogenic effects, whereas above $\rho \leq 0.4$, degradation facilitates sprout progression.

In these studies, we isolate and examine variations in fiber density and structure, and proteolytic matrix degradation as independent mechanisms that control vascular morphogenesis. However, the integrin, protease, and growth factors systems are highly connected and provide regulatory feed-

back for each other (53). Thus, there is still a need for more in depth investigations on the relationship between extracelluar stimuli and cellular function. In particular, studies focusing on intracellular signaling and cross-talk between the integrin and growth factor receptors are of key importance.

Acknowledgments
This work was performed at Los Alamos National Laboratory as part of the PhD dissertation research of ALB and was supported in part by the U.S. Department of Energy under Contract No. DE-AC52-06NA25396. TLJ was supported in part by the Alfred P. Sloan Foundation and the James S. McDonnell Foundation.

References

1. Czirok, A., E. A. Zamir, M. B. Filla, C. D. Little, and B. J. Rongish. 2006. Extracellular matrix macroassembly dynamics in early vertebrate embryos. *Curr. Top. Dev. Biol.* 73:237 – 258.

2. Midwood, K. S., L. V. Williams, and J. E. Schwarzbauer. 2004. Tissue repair and the dynamics of the extracellular matrix. *Int. J. Biochem. Cell Biol.* 36:103 – 1037.

3. Davis, G. E., and D. R. Senger. 2005. Endothelial extracellular matrix: Biosynthesis, remodeling, and functions during vascular morphogenesis and neovessel stabilization. *Circ. Res.* 97:1093 – 1107.

4. Ruoslahti, E. 1992. Control of cell motility and tumor invasion by extracellular matrix interactions. *Br. J. Cancer* 66:239 – 242.

5. Alberts, B., D. Bray, J. Lewis, M. Raff, K. Roberts, and J. D. Watson. 2002. Molecular Biology of the Cell. 4th edition. Garland Science, New York.

6. Laurent, G. J. 1987. Dynamic state of collagen: pathways of collagen degradation in vivo and their possible role in regulation of collagen mass. *Am. J. Physiol., Cell Physiol.* 252:C2 – C9.

7. Silver, F. H., J. W. Freeman, and G. P. Seehra. 2003. Collagen self-assembly and the development of tendon mechanical properties. *J. Biomech.* 36:1529 – 1553.

8. Friedl, P., and E. B. Bröcker. 2000. The biology of cell locomotion within three-dimensional extracellular matrix. *Cell. Mol. Life Sci.* 57:41 – 64.

9. Rupp, P. A., and C. D. Little. 2001. Integrins in vascular development. *Circ. Res* 89:566 – 572.

10. Martinez-Lemus, L. A., X. Wu, E. Wilson, M. A. Hill, G. E. Davis, M. J. Davis, and G. A. Meininger. 2003. Integrins as unique receptors for vascular control. *J. Vasc. Res.* 40:211 – 233.

11. Schwartz, M. A., M. D. Schaller, and M. H. Ginsberg. 1995. Integrins: Emerging paradigms of signal transduction. *Annu. Rev. Cell Dev. Biol.* 11:549 – 599.

12. Nobes, C. D., and A. Hall. 1995. Rho, rac, and cdc42 GTPases regulate the assembly of multimolecular focal complexes associated with actin stress fibers, lamellipodia, and filopodia. *Cell* 18:53 – 62.

13. Chen, C. S., M. Mrksich, S. Huang, G. M. Whitesides, and D. E. Ingber. 1998. Micropatterned surfaces for control of cell shape, position, and function. *Biotechnol. Prog.* 14:356 – 363.

14. Tranquillo, R. T. 1999. Self-organization of tissue-equivalents: the nature and role of contact guidance. *Biochem. Soc. Symp.* 65:27 – 42.

15. Chicurel, M. E., C. S. Chen, and D. E. Ingber. 1998. Cellular control lies in the balance of forces. *Curr. Opin. Cell Biol.* 10:232 – 239.

16. Huang, S., and D. E. Ingber. 1999. The structural and mechanical complexity of cell-growth control. *Nat. Cell Biol.* 1:E131 – E138.

17. Vernon, R. B., and E. H. Sage. 1995. Between molecules and morphology: extracellular matrix and the creation of vascular form. *Am. J. Pathol.* 147:873 – 883.

18. Vernon, R. B., J. C. Angello, M. L. Iruela-Arispe, T. F. Lane, and E. H. Sage. 1992. Reorganization of basement membrane matrices by cellular traction promotes the formation of cellular networks *in vitro*. *Lab. Invest.* 66:536 – 547.

19. Roeder, B. A., K. Kokini, B. Z. Waisner, J. E. Sturgis, J. P. Robinson, and S. L. Voytik-Harbin. 2003. Extracellular matrix microstructure determines ecm-cell strain transfer in 3D tissue constructs. *In* 2003 Summer Bioengineering Conference, Key Biscayne, Florida, USA.

20. Discher, D. E., P. Janmey, and Y. Wang. 2005. Tissue cells feel and respond to the stiffness of their substrate. *Science* 310:1139 – 1143.

21. Korff, T., and H. G. Augustin. 1999. Tensional forces in fibrillar extracellular matrices control directional capillary sprouting. *J. Cell Sci.* 112:3249 – 3258.

22. Friedl, P., Y. Hegerfeldt, and M. Tusch. 2004. Collective cell migration in morphogenesis and cancer. *Int. J. Dev. Biol.* 48:441 – 449.

23. Nakahara, H., L. Howard, E. W. Thompson, H. Seiki, M. Sato, Y. Yeh, and W. Chen. 1997. Transmembrane/cytoplasmic domain-mediated membrane type 1-matrix metalloproteinase docking to invadopodia is required for cell invasion. *Proc. Natl. Acad. Sci.* 94:7959 – 7964.

24. Krishnan, L., H. Ngyuen, H. Song, J. B. Hoying, and J. A. Weiss. 2005. Gene expression in a 3-dimensional model of angiogenesis: Relation to matrix mechanical properties. *In* 2005 Summer Bioengineering Conference, Vail, Colorado, USA.

25. Mantzaris, N. V., S. Webb, and H. G. Othmer. 2004. Mathematical modeling of tumor-induced angiogenesis. *J. Math. Biol.* 49:111 – 187.

26. Houck, K. A., D. W. Leung, A. M. Rowland, J. Winer, and N. Ferrara. 1992. Dual regulation of vascular endothelial growth factor bioavailability by genetic and proteolytic mechanisms. *J. Biol. Chem.* 267:26031 – 26037.

27. Lee, S., S. M. Jilani, G. V. Nikolava, D. Carpizo, and M. L. Iruela-Arispe. 2005. Processing of VEGF-A by matrix metalloproteinases regulates bioavailability and vascular patterning in tumors. *J. Cell Biol.* 169:681 – 691.

28. Ausprunk, D. H., and J. Folkman. 1977. Migration and proliferation of endothelial cells in preformed and newly formed blood vessels during tumor angiogenesis. *Microvasc. Res.* 14:53 – 65.

29. Muthukkaruppan, V. R., L. Kubai, and R. Auerbach. 1982. Tumor-induced neovascularization in the mouse eye. *J. Natl. Cancer Inst.* 69:699 – 704.

30. Lo, C., H. Wang, M. Dembo, and Y. Wang. 2000. Cell movement is guided by the rigidity of the substrate. *Biophys. J.* 79:144 – 152.

31. Kaufman, L. J., C. P. Brangwynne, K. E. Kasza, E. Filippidi, V. D. Gordon, T. S. Deisboeck, and D. A. Weitz. 2005. Glioma expansion in

collagen i matrices: analyzing collagen concentration-dependent growth and motility patterns. *Biophys. J.* 89:635 – 650.

32. Levick, J. R. 1987. Flow through interstitium and other fibrous matrices. *Q. J. Exp. Physiol.* 72:409 – 437.

33. Bauer, A. L., T. L. Jackson, and Y. Jiang. 2007. A cell-based model exhibiting branching and anastomosis during tumor-induced angiogenesis. *Biophys. J.* 92:3105–3121.

34. Paweletz, N., and M. Knierim. 1989. Tumor related angiogenesis. *Crit. Rev. Oncol. Hematol.* 9:197 – 242.

35. Kearney, J. B., N. C. Kappas, C. Ellerstrom, F. W. DiPaola, and V. L. Bautch. 2004. The VEGF receptor flt–1 (VEGFR–1) is a positive modulator of vascular sprout formation and branching morphogenesis. *Blood* 103:4527 – 4535.

36. Sholley, M. M., G. P. Ferguson, H. R. Seibel, J. L. Montour, and J. D. Wilson. 1984. Mechanisms of neovascularization. vascular sprouting can occur without proliferation of endothelial cells. *Lab. Invest.* 51:624 – 634.

37. Gerhardt, H., M. Golding, M. Fruttiger, C. Ruhrberg, A. Lundkvist, A. Abramsson, M. Jeltsch, C. Mitchell, K. Alitalo, D. Shima, and C. Betsholtz. 2003. VEGF guides angiogenic sprouting utilizing endothelial tip cell filopodia. *J. Cell Biol.* 161:1163 – 1177.

38. Williams, S. K. 1987. Isolation and culture of microvessel and large-vessel endothelial cells; their use in transport and clinical studies. *In* Microvascular Perfusion and Transport in Health and Disease, P. F. McDonagh, editor. S. Karger AG, Basel, Switzerland, 204 – 245.

39. Serini, G., D. Ambrosi, E. Giraudo, A. Gamba, L. Preziosi, and F. Bussolino. 2003. Modeling the early stages of vascular network assembly. *EMBO J.* 22:1771 – 1779.

40. Carmeliet, P. 2005. VEGF as a key mediator of angiogenesis in cancer. *Oncology* 69:4 – 10.

41. Gabhann, F. M., and A. S. Popel. 2004. Model of competitive binding of vascular endothelial growth factor and placental growth factor to VEGF receptors on endothelial cells. *Am. J. Physiol. Heart Circ. Physiol.* 286:153 – 164.

42. Wang, D., R. E. Lehman, D. B. Donner, M. R. Matli, R. S. Warren, and M. L. Welton. 2002. Expression and endocytosis of VEGF and its receptors in human colonic vascular endothelial cells. *Am. J. Physiol. Gastrointest. Liver Physiol.* 282:1088 – 1096.

43. Leith, J. T., and S. Michelson. 1995. Secretion rates and levels of vascular endothelial growth factor in clone A or HCT-8 human colon tumour cells as a function of oxygen concentration. *Cell Prolif.* 28:415 – 430.

44. Jiang, Y., J. Pjesivac-Grbovic, C. Cantrell, and J. P. Freyer. 2005. A multiscale model for avascular tumor growth. *Biophys. J.* 89:3884 – 3894.

45. Gimbrone, M. A., R. S. Cotran, S. B. Leapman, and J. Folkman. 1974. Tumor growth and neovascularization: an experimental model using the rabbit cornea. *J. Natl. Cancer Inst.* 52:413 – 427.

46. Czirok, A., E. D. Perryn, and A. Czirok. 2007. Network formation of tissue cells via preferential attraction to elongated structures. *PRL* 98:038102: 1–4.

47. Sun, S., M. F. Wheeler, M. Obeyesekere, and C. W. Patrick. 2005. A deterministic model of growth-factor induced angiogenesis. *Bull. Math. Biol.* 67:131 – 337.

48. Demuth, T., and M. E. Berens. 2004. Molecular mechanisms of glioma cell migration and invasion. *J. Neurooncol.* 70:217 – 228.

49. Ingber, D. E., and J. Folkman. 1989. Mechanochemical switching between growth and differentiation during fibroblast growth factor-stimulated angiogenesis *in vitro*: role of extracellular matrix. *J. Cell Biol.* 109:317 – 330.

50. Shiu, Y., S. Li, W. A. Marganski, S. Usami, M. A. Schwartz, Y. Wang, M. Dembo, and S. Chien. 2004. Rho mediates the shear enhancement of endothelial cell migration and traction force generation. *Biophys. J.* 86:2558 – 2565.

51. Forgacs, G. 1995. On the possible role of cytoskeletal filamentous networks in intracellular signaling: an approach based on percolation. *J. Cell Sci.* 108:2131 – 2143.

52. Anderson, A. R. A., and M. A. J. Chaplain. 1998. Continuous and discrete mathematical models of tumor-induced angiogenesis. *Bull. Math. Biol.* 60:857 – 900.

53. Gagne, P., A. Akalu, and P. C. Brooks. 2004. Challenges facing antiangiogenic therapy for cancer: impact of the tumor extracelluar environment. *Expert Rev. Anticancer Ther.* 4:129 – 140.

54. Keshet, E., and S. A. Ben-Sasson. 1999. Anticancer drug targets: approaching angiogenesis. *J. Clin. Invest.* 104:1497 – 1501.

55. Oakley, C., N. A. F. Jaeger, and D. M. Brunette. 1997. Sensitivity of fibroblasts and their cytoskeletons to substratum topographies: Topographic guidance and topographic compensation by micromachined grooves of different dimensions. *Exp. Cell Res.* 234:413 – 424.

Table 1: Table of Parameters. Dimensions are given in terms of L=length, T=time, M=mass and E=energy. Unless otherwise noted, all simulations used the same parameter set and initial conditions. EC denotes endothelial cell.

Parameter	Symbol	Dimensions	Model Value
Length Scales	l_1, l_2	L	166μm, 106μm
VEGF Diffusion	D	L^2/T	3.6x10^{-4} cm^2/h (39)
VEGF Decay	λ	T^{-1}	.6498 h^{-1} (39)
VEGF Uptake	β	M/cell/T	.06 pg/EC/hr (40–42)
VEGF Source	S	M/L	.035 pg/pixel (43, 44)
Activation Threshold	v_a	M	.0001 pg
Adhesion			
EC−EC	J_{ee}	E/L	30
EC−Fluid	J_{ef}	E/L	76
EC−Matrix	J_{em}	E/L	66
Fluid−Fluid	J_{ff}	E/L	71
Fluid−Matrix	J_{fm}	E/L	85
Matrix−Matrix	J_{mm}	E/L	85
Membrane Elasticty			
EC	γ_{e}	E/L^4	0.8
Matrix	γ_{m}	E/L^4	0.5
Fluid	γ_{f}	E/L^4	0.5
Chemotactic Sensitivity	χ	E/conc	$1.11 \cdot 10^6$
Tip Cell		E/conc	$-1.45\,\chi$
Stalk Cell		E/conc	$-1.42\,\chi$
Proliferating Cell		E/conc	$-1.40\,\chi$
Intracellular Adhesion	α	E/L	300
Boltzmann Temperature	kT	E	2.5

Figure Legends

Figure 1.

The average extension speeds of our simulated sprouts agree with the empirical measurements (35, 45). Parameters were chosen to maximize extension speeds. Reported speeds are an average of 10 independent simulations using the same parameter set. Error bars represent the standard error from the mean. The inset shows the geometry of the computational domain and simulated sprout development. Endothelial cells (red) have migrated into the domain from a parent blood vessel (left boundary); a source of growth factor is available and diffuses from the right boundary. The space between represents the stroma and is composed of extracellular matrix fibers (green) and interstitial fluid (blue). Snapshot at 7.8 hours.

Figure 2.

For a different parameter set, fewer cells are recruited from the parent vessel and cells elongate. Here cells are approximately 40 μm in length and the average extension speed at 14 hours is 6.8 μm/hr. $J_{\{ee,em,ef\}}=\{42,76,66\}$, $\chi_{\text{tip}} = 1.55\,\chi$, $\chi_{\{\text{migr,prolif}\}} = 1.45\,\chi$.

Figure 3.

Panel (a): Fibroblasts stained for actin (e) and tubulin (f) showing that cells alter their shape, orientation, and polarity to align with the direction of the grooves (double-headed arrow). Images reprinted from (55) with permission from Elsevier. Compare with panel (b), which is a simulation of the cellular response to topographical guidance on similarly patterned substratum and demonstrates the flexibility of our model to capture a variety of different morphological phenomena.

Figure 4.

Panel (a) shows the dependence of average sprout extension speed on the density of the extracellular matrix. The model predicts that average extension speeds are maximal in the fiber fraction range $\rho = 0.3 - 0.4$. Above $\rho = 0.6$, extension speeds are significantly reduced and for $\rho < 0.1$ and $\rho > 0.8$ normal angiogenesis is interrupted suggesting that modulating matrix density may be an effective anti-angiogenesis therapy. Panel (b) quantifies morphological properties of the sprout showing sprout thicknesses in

normal physiological ranges and a distinct range of fiber density conductive to branching.

Figure 5.

Plots showing the effect of the mechanical properties of the ECM, such as fiber anisotropies and matrix malleability, on sprout morphology and viability. Snapshots at 14 hours. From top left to bottom right: (a) $\rho = 0.05$. Interruption of normal angiogenesis and loss of sprout viability, (b) $\rho = 0.2$. High matrix anisotropy induces branching and (c) $\rho = 0.25$ anastomosis/lumen formation, (d) $\rho = 0.6$. Homogeneous matrix fiber network produces linear sprouts, (e) $\rho = 0.7$. Matrix more malleable and less tension transferred to cells results in wider and slower sprout formation, (f) $\rho = 0.99$. Complete inhibition of angiogenesis at high matrix density.

Figure 6.

Evidence that mechanical cues, or contact guidance, from the ECM affects sprout extension. At $\rho = \{0.4, 0.6\}$, rates of sprout extension are more rapid when matrix fibers are aligned with VEGF gradients ($0°$) than when matrix fibers are aligned perpendicular to the gradient ($90°$).

Figure 7.

Sprouts developing on patterned matrices reveal a strong correspondence between fiber alignment and cell shape and orientation. The sprouts migrate toward higher concentrations of VEGF, however, cells elongate and are clearly oriented in the direction of the matrix cords. These results demonstrate the important role of contact guidance and tissue structure in determining cell shape and orientation. Snapshots at 12.5 hours.

Figure 8.

This plot shows that the effect of matrix degradation on average sprout extension speeds depends on the density of the ECM. Solid lines represent average extension speeds without matrix degradation and the corresponding colored dashed lines show average speeds with tip cell matrix degradation. For $\rho \leq 0.25$, matrix degradation has anti-angiogenic effects. Above $\rho = 0.4$, degradation facilitates sprout progression.

Figure 9.

Without degradation, angiogenesis is inhibited at $\rho = 0.99$ (Figure 5f). Panel (a) shows that tip cell matrix degradation promotes sprout development at $\rho = 0.99$ by carving out a path for migration. Panel (b) depicts sprout formation with ECM degradation at $\rho = 0.4$ and suggests that high matrix anisotropy created by tip cell degradation may be a mechanism for branching. Snapshot at 14 hours.

Figure 10.

Plot showing the effect of varying the chemotactic sensitivity parameter on average sprout extension speed at 14 hours. Below $\chi = 1 \cdot 10^4$ chemotactic forces are not strong enough relative to the energies associated with adhesion and growth to induce motility. Above $\chi = 1.6 \cdot 10^6$, chemotactic forces are strong enough relative to adhesion and growth that the cells dissociate.

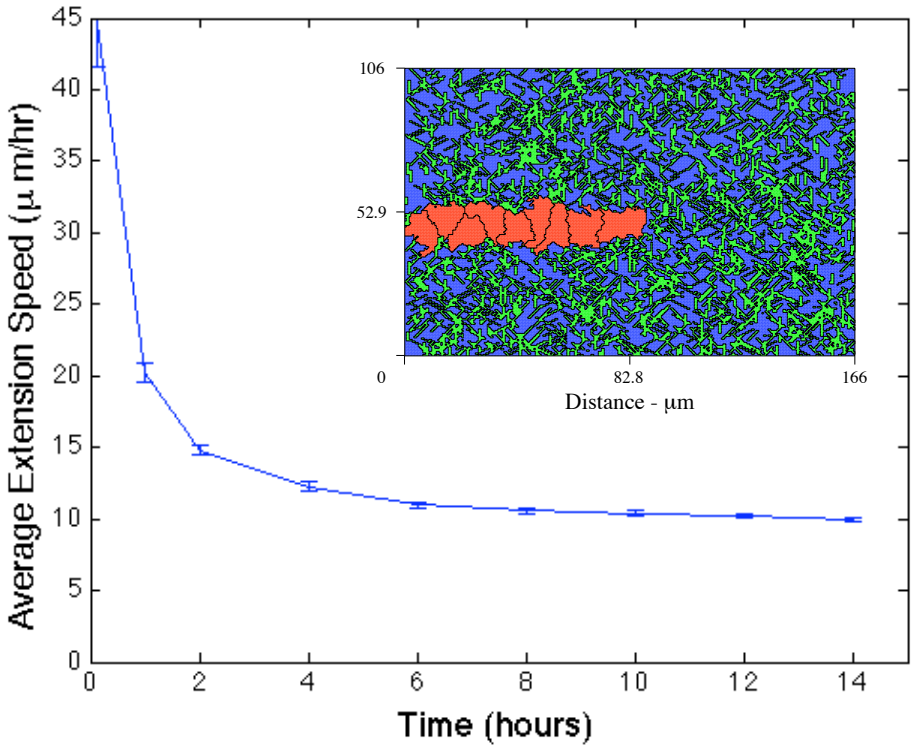
Average Extension Speed (μ m/hr)
Time (hours)
0
5
10
15
20
25
30
35
40
45
0
2
4
6
8
10
12
14
106
52.9
0
82.8
166
Distance - μm

Figure 1:

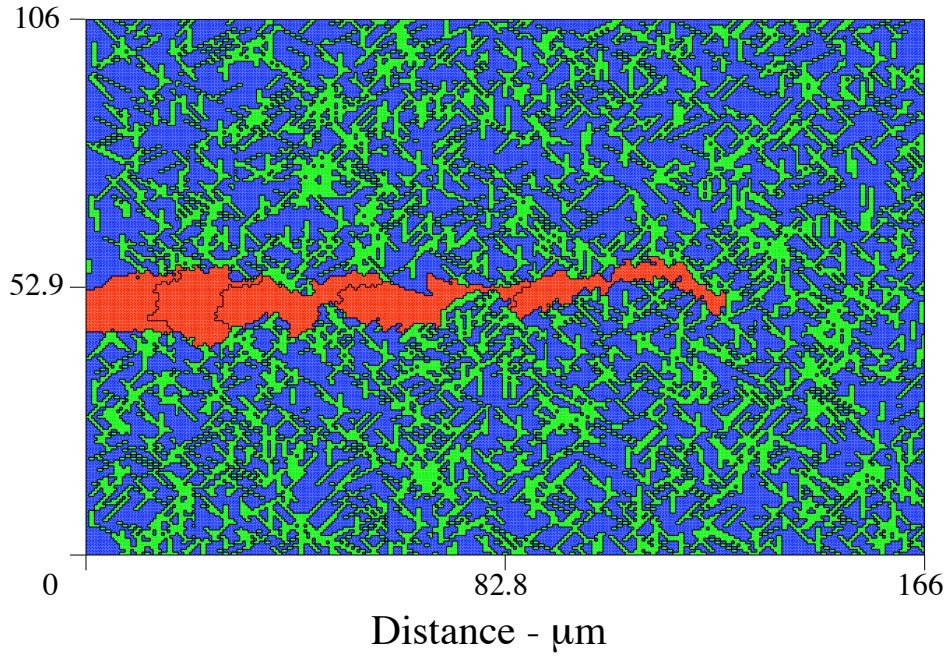

Figure 2:

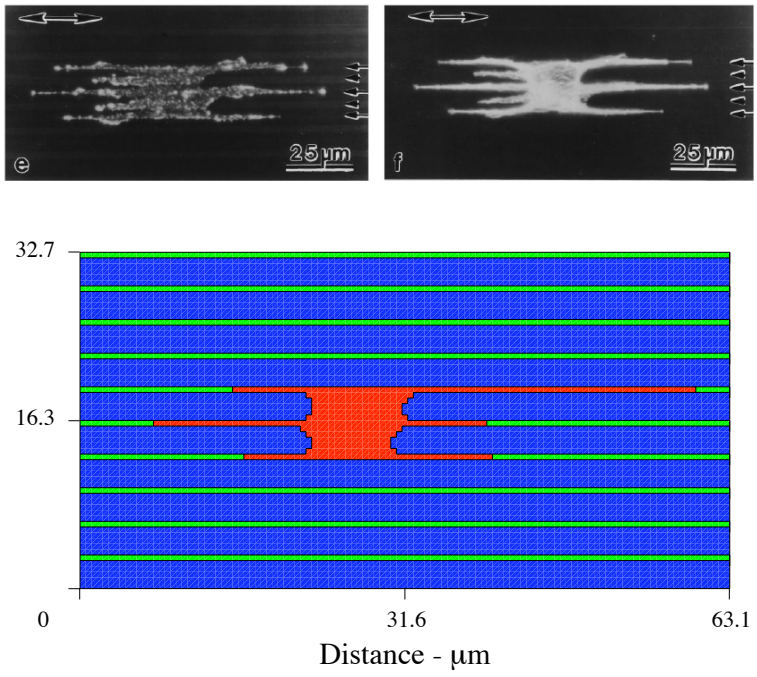

Figure 3:

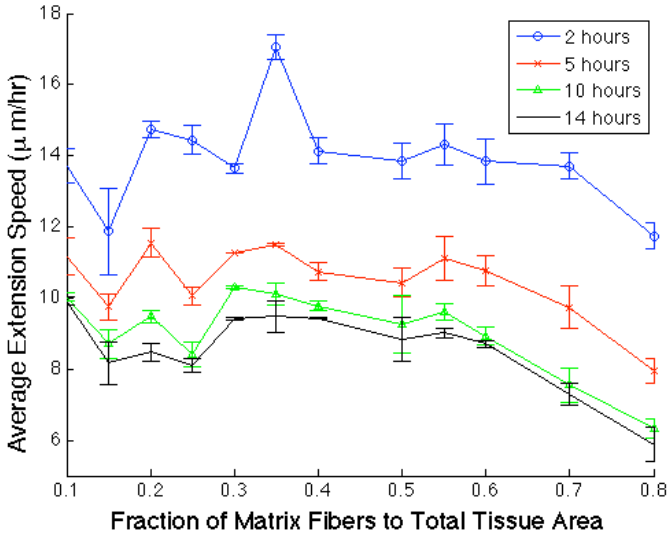
2 hours
5 hours
10 hours
14 hours
Average Extension Speed (μm/hr)
Fraction of Matrix Fibers to Total Tissue Area
18
16
14
12
10
8
6
0.1
0.2
0.3
0.4
0.5
0.6
0.7
0.8

(a)

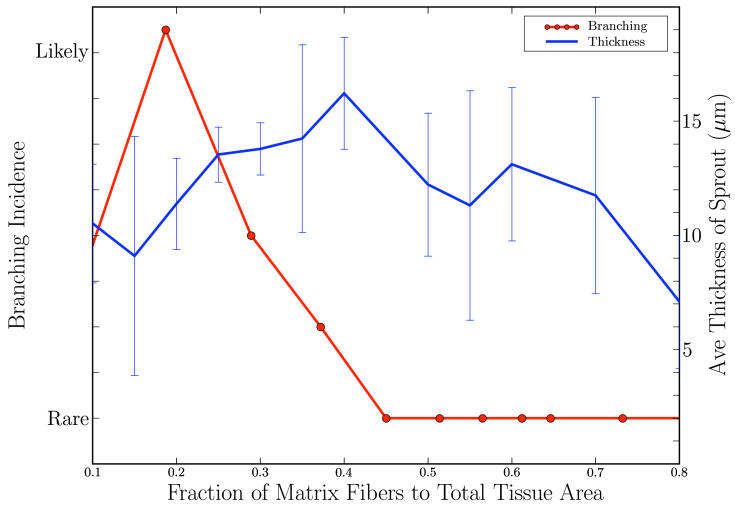
Branching
Thickness
Likely
Rare
Branching Incidence
Ave Thickness of Sprout (μm)
Fraction of Matrix Fibers to Total Tissue Area
15
10
5
0.1
0.2
0.3
0.4
0.5
0.6
0.7
0.8

(b)

Figure 4:

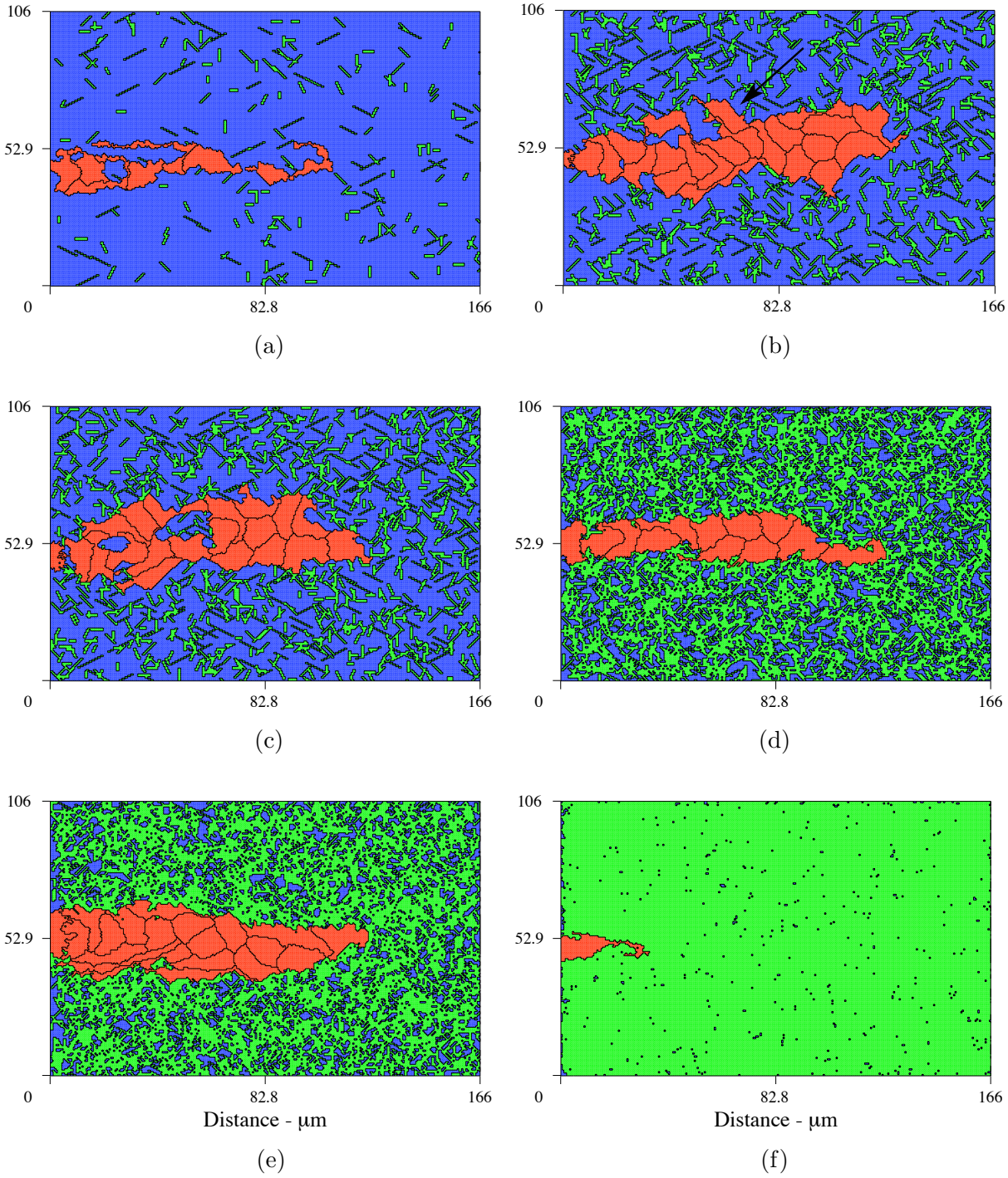

Figure 5:

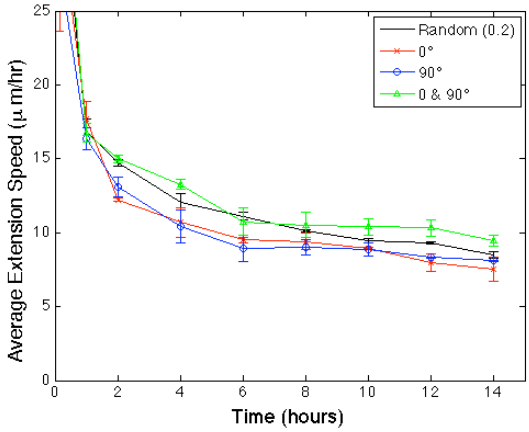
Random (0.2)
0°
90°
0 & 90°
Average Extension Speed (μm/hr)
Time (hours)

(a)

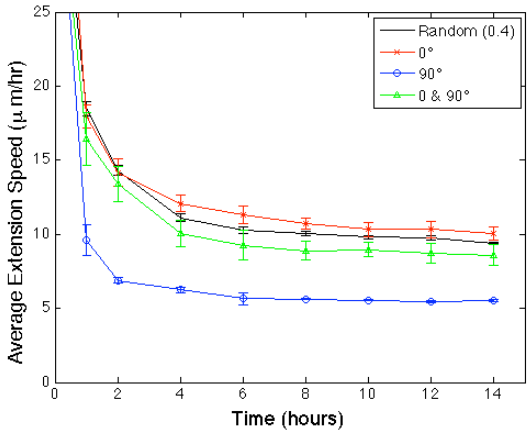
Random (0.4)
0°
90°
0 & 90°
Average Extension Speed (μm/hr)
Time (hours)

(b)

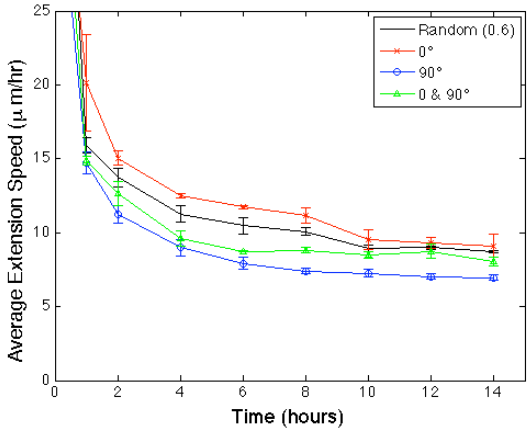
Random (0.6)
0°
90°
0 & 90°
Average Extension Speed (μm/hr)
Time (hours)

(c)

Figure 6:

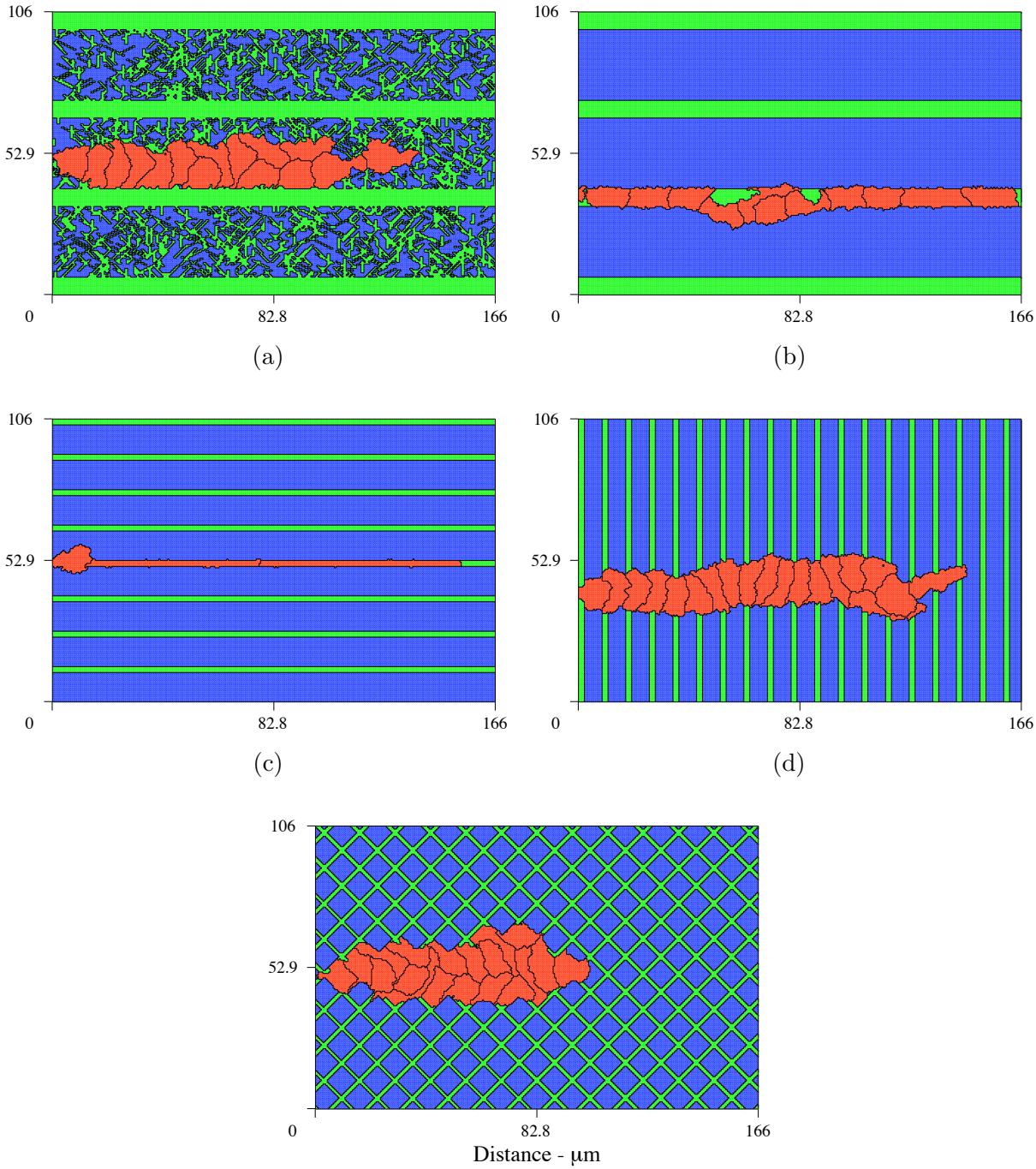

Figure 7:

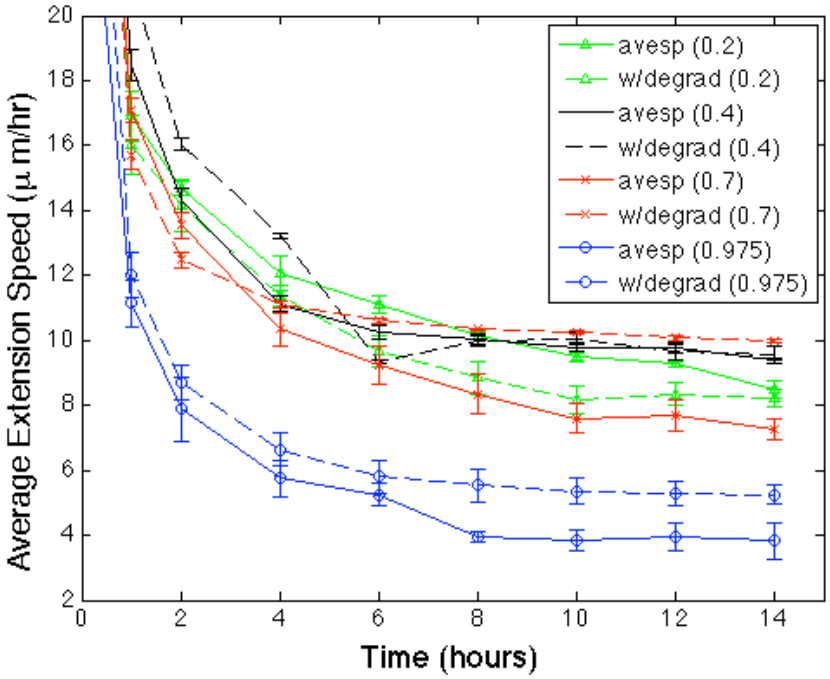
Average Extension Speed (μ m/hr)
Time (hours)
avesp (0.2)
w/degrad (0.2)
avesp (0.4)
w/degrad (0.4)
avesp (0.7)
w/degrad (0.7)
avesp (0.975)
w/degrad (0.975)
20
18
16
14
12
10
8
6
4
2
0
2
4
6
8
10
12
14

Figure 8:

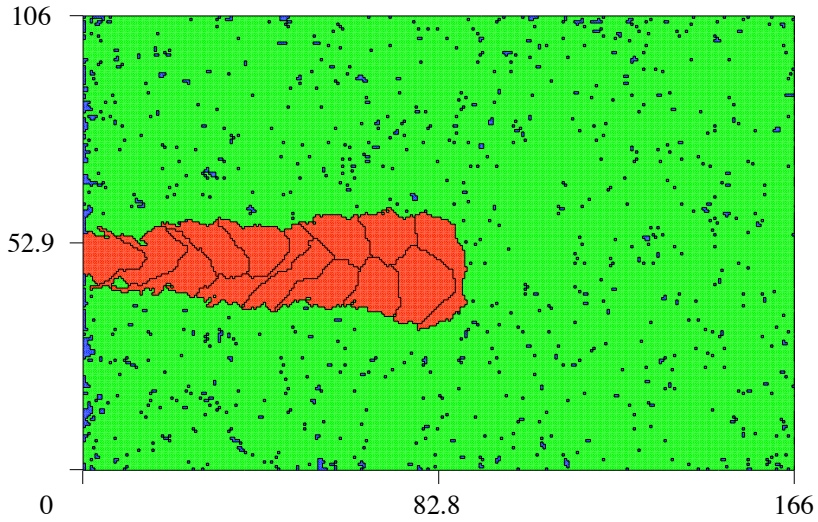

(a)

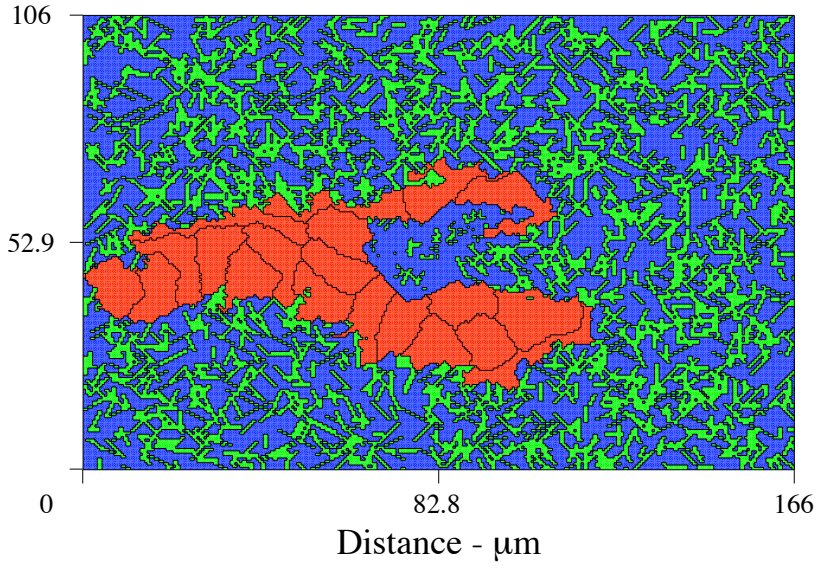

(b)

Figure 9:

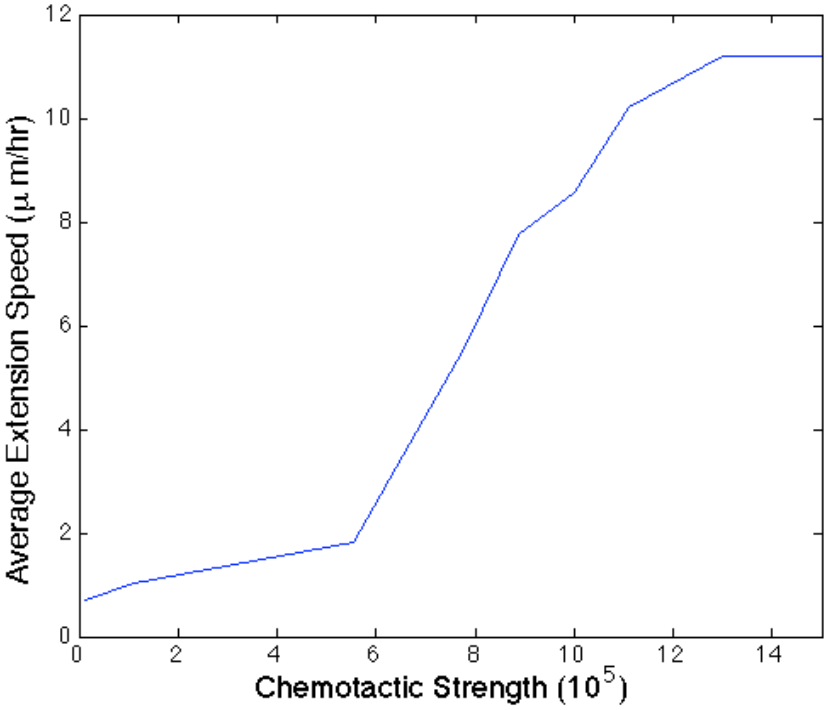
Average Extension Speed (μm/hr)
Chemotactic Strength (10^5)
0
2
4
6
8
10
12
14

Figure 10: